

Full paper



## High-temperature-pulse synthesis of ultrathin-graphene-coated metal nanoparticles

Hua Xie<sup>a,1</sup>, Yifan Liu<sup>b,1</sup>, Na Li<sup>c,1</sup>, Boyang Li<sup>d,1</sup>, Dylan J. Kline<sup>e</sup>, Yonggang Yao<sup>a</sup>, Michael R. Zachariah<sup>e</sup>, Guofeng Wang<sup>d,\*</sup>, Dong Su<sup>c,\*</sup>, Chao Wang<sup>b,\*</sup>, Liangbing Hu<sup>a,\*</sup>

<sup>a</sup> Department of Materials Science and Engineering, University of Maryland, College Park, MD, 20742 USA

<sup>b</sup> Department of Chemical and Biomolecular Engineering, Johns Hopkins University, Baltimore, MD, 21218 USA

<sup>c</sup> Center for Functional Nanomaterials, Brookhaven National Laboratory, Upton, NY 11973 USA

<sup>d</sup> Department of Mechanical Engineering and Materials Science, University of Pittsburgh, Pittsburgh, PA 15261 USA

<sup>e</sup> Department of Chemical and Biomolecular Engineering and Chemistry and Biochemistry, University of Maryland, College Park, MD, 20742 USA

### ARTICLE INFO

#### Keywords:

Nanoparticles  
High temperature  
Rapid synthesis  
Core-shell structure  
Graphene

### ABSTRACT

Nanomaterials comprising earth-abundant elements show great potential as substitutes for scarce, expensive materials in energy conversions, but degradation and contamination issues in working environments severely limit their practical applications. Here we report a facile and scalable strategy to synthesize ultrathin-graphene-coated cobalt nanoparticles which are achieved by the application of an electrical current pulse to a carbon-based substrate and by generating a transient high temperature of up to 1500 K in 50 ms to induce the nanoparticle growth and graphene coating. Thickness of the graphene shell is effectively controlled to be under three atomic layers, favorable for charge transfer and electrocatalytic applications. Our one-step synthetic strategy provides a universal, scalable and cost-effective approach for the fast synthesis of metal-carbon core-shell nanoarchitectures for energy conversion applications.

### 1. Introduction

Global sustainability gives strong impetus towards the innovation of materials for energy storage and conversion; consequently, developments in nanotechnology have burgeoned and strived to meet the demanding technological requirements over the past decades. Materials with nanostructures possess attractive properties such as remarkably high chemical activities and enhanced electron-transfer capabilities, which are promising for energy storage [1,2], nanoelectronics [3,4], as well as electrocatalysis [5–8]. Noble elements are preferred for many specific energy conversion reactions because of their excellent catalytic performance [9–14], however, their high prices have forced researchers to develop and explore alternatives composed of more economically-viable transition metals [15–20]. Despite the promise of transition metal nanomaterials, several drawbacks have impeded their long-term utilization toward energy-related applications. One of the most challenging problems is stability, in which degradation in the form of agglomeration, morphological transformations, and detachment from the substrate, can lead to degraded properties and even deactivation.

Contamination is another important issue that occurs especially when the active sites, such as specific lattice planes, are exposed to toxic environments. To address these issues, various approaches have been undertaken to bolster the chemical stability and electrocatalytic durability. A typical approach is to form a protective shell of organic molecules or carbon [21,22]. However, many of these structures involve complicated operations, or the protective coatings are undesirably thick, hindering the effective reaction pathway, which severely impairs the performance of the nanomaterials.

To protect nanomaterial morphology and to retain their chemical stability and electrocatalytic durability, an innovative yet simple synthetic technique can circumvent these limitations. Therefore, a robust, low-cost and scalable Joule heating method of creating ultrathin and durable coating layers on nanoparticles is introduced in this work. Here, we synthesize metallic nanoparticles with a desired thickness of graphene layers by applying one single high-temperature pulse to metal-precursor-loaded carbon substrates. No complicated organic materials were exploited for the formation of the ultrathin graphene shells. Amorphous carbon sources, such as carbonized nanofibers or carbonized

\* Corresponding authors.

E-mail addresses: [guw8@pitt.edu](mailto:guw8@pitt.edu) (G. Wang), [dsu@bnl.gov](mailto:dsu@bnl.gov) (D. Su), [chaowang@jhu.edu](mailto:chaowang@jhu.edu) (C. Wang), [binghu@umd.edu](mailto:binghu@umd.edu) (L. Hu).

<sup>1</sup> These authors contributed equally to this work.

wood, act as reservoirs which supply carbon atoms towards the formation of ultrathin graphene shells. Tuning both the pulse temperature and time enables precise control over the shells to fewer than three graphene layers. Our strategy presents several advantages: (1) the procedure successfully fabricates core-shell nanostructures in one facile step; (2) shell thickness can be effectively tuned to under three atomic layers; (3) this unique approach facilitates control over material design, where an abundance of substrates and precursor salts can be used. The enhanced chemical stability and electrocatalytic durability of the resultant core-shell nanoparticles are advantageous for a diverse array of applications.

Our synthesis strategy is briefly illustrated in Fig. 1, which schematically reveals the fabrication process of graphene/transition metal core-shell nanoparticles. Cobalt(II) chloride ( $\text{CoCl}_2 \cdot 6\text{H}_2\text{O}$ ) was exploited as a precursor salt loaded onto carbon-based supports through solution-based processing. Note that the substrates, such as carbon nanofibers (CNF) and carbonized wood, are readily available and easily manufacturable. A controlled transient current was applied to the conductive substrate with a time span of 50 ms to instantaneously raise the localized temperature to approximately 1500 K. The high temperature achieved provides the energy necessary to decompose the  $\text{CoCl}_2$  precursor and to form Co clusters. Meanwhile, carbon atoms from the substrate are also supplied enough energy to detach locally from the substrate. Rapid quenching occurs after the high temperature pulse at a rate of  $\sim 30,000$  K/s, which enables the formation of non-agglomerated core-shell nanoparticles anchored to the defective sites of the carbon substrates. It is supposed that the Co nanoparticle cores function as catalysts aiding the epitaxial growth of the ultrathin graphene shells, which resembles the fabrication of graphene by chemical vapor deposition (CVD) [23,24]. The ultrathin graphene shell acts as a citadel to separate the nanoparticles to inhibit the agglomeration, to protect Co nanoparticles from contamination, as well as to anchor firmly the nanoparticles on the substrate, while still allowing electrons from oxygen to penetrate the thin graphene and react with the Co nanoparticles.

Details of the high-temperature pulse experiment can be found in the Supporting Information (Methods and Fig. S1). Fig. 2a and b present the typical morphological evolution of the samples before and after the high temperature pulse. After the high temperature pulse, Co nanoparticles coated with graphene are homogeneously anchored onto the CNF (Fig. 2b). Transmission electron microscopy (TEM) images, shown in Fig. 2c, are typical examples of Co nanoparticles with coatings of 1–3 graphene layers respectively. Dimensional statistics of the nanoparticles (Fig. 2d) conform to a typical Gaussian distribution with particle diameters ranging from 4 nm to 30 nm. Fig. 2e illustrates the distribution for the core-shell nanoparticles produced by the high temperature pulse technique, with characteristic graphene shells from 1 to 3 layers thick.

It is noted that a strong correlation between the number of graphene layers and the nanoparticle size can be found based on the statistics: the nanoparticles with smaller size tend to maintain a single graphene layer,

whereas bilayer and trilayer graphene shells are often observed for relative larger nanoparticles (Fig. S2). This interesting phenomenon offers insight into the rearrangement mechanism of the carbon/Co clusters during the transient high temperature exposure. Our hypothesis is that the quench rate has an influence on the layer numbers, as a slow cooling rate can extend the carbon atom deposition process on the surface of nanoparticles. As a result, more carbon atoms were stacked to form thicker graphene layers, along with the growth of nanoparticles. The hypothesis may explain the correlation between the graphene layer number and particle dimensions, which further prove that the graphene thickness is controllable with this technique. We tuned the processing parameters and employed a high temperature pulse with a prolonged duration around 500 ms. Accordingly, the metallic clusters become agglomerated with nanoparticles on the order of 100 nm in diameter. As expected, the graphene shell increases in thickness to approximately 10 layers (Fig. S3). Note that the graphitization of carbon atoms is also influenced by the pulsing temperature, since high temperature can help the graphitization process, while lower local temperature decreases the kinetics and is not elevated enough to furnish migration energy to form crystallized graphitic structure. As a result, a thick amorphous carbon coating can be observed on the surface of the Co nanoparticles after a prolonged thermal pulse (Fig. S4). Fig. 2f illustrates the X-ray diffraction pattern in which peaks at  $44.22^\circ$ ,  $51.52^\circ$ , and  $75.85^\circ$  are attributed to the (111), (200), and (220) planes of the Co nanoparticles, corresponding to a face centered cubic (fcc) structure ( $\text{Fm}\bar{3}\text{m}$ ). The peaks correspond well with our simulation result for an average particle size of 15 nm (Fig. S5). Note that cubic Co is the high temperature phase which can be successfully preserved due to the rapid quenching process ( $\sim 30,000$  K/s). The graphene-coated Co nanoparticles also exhibit good chemical stability, as no obvious oxidation was observed after 2 h heat treatment in air at  $200^\circ\text{C}$  (Fig. S6).

Fig. 3a depicts high resolution (HR-) TEM analysis, together with the selected area electron diffraction pattern (Fig. 3b) showing that the Co nanoparticles are cubic (fcc) structure, which coincides with the aforementioned XRD pattern. X-ray photoelectron spectroscopy (XPS) spectra of the core-shell supported nanoparticles are shown in Fig. 3c. The characteristic Co peaks confirm the formation of metallic Co nanoparticles from the precursor salt (Co atomic ratio: around 3.2%). Fig. 3d presents the electron energy-loss spectroscopy (STEM-EELS) elemental mappings of the Co@graphene nanoparticles. It is evident that the nanoparticles formed by high temperature pulse are core-shell structures, with cobalt and carbon atoms displayed in red and green, respectively. We can assume that the Co nanoparticles act as catalytic centers, which promotes the growth of graphene layers epitaxially on the nanoparticle surface. Specifically, melamine can be added in the precursor as a nitrogen source to realize nitrogen doping. XPS analysis was employed to differentiate the composition variation of nitrogen for samples with and without N-doping (Fig. S7). The sample from precursors with melamine as N-source presents a significant increase in

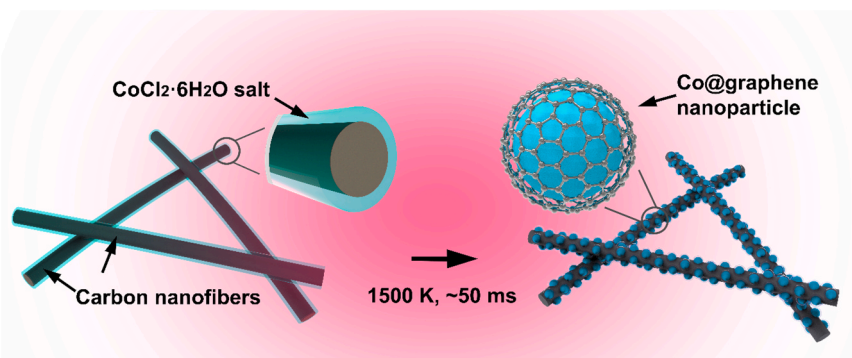
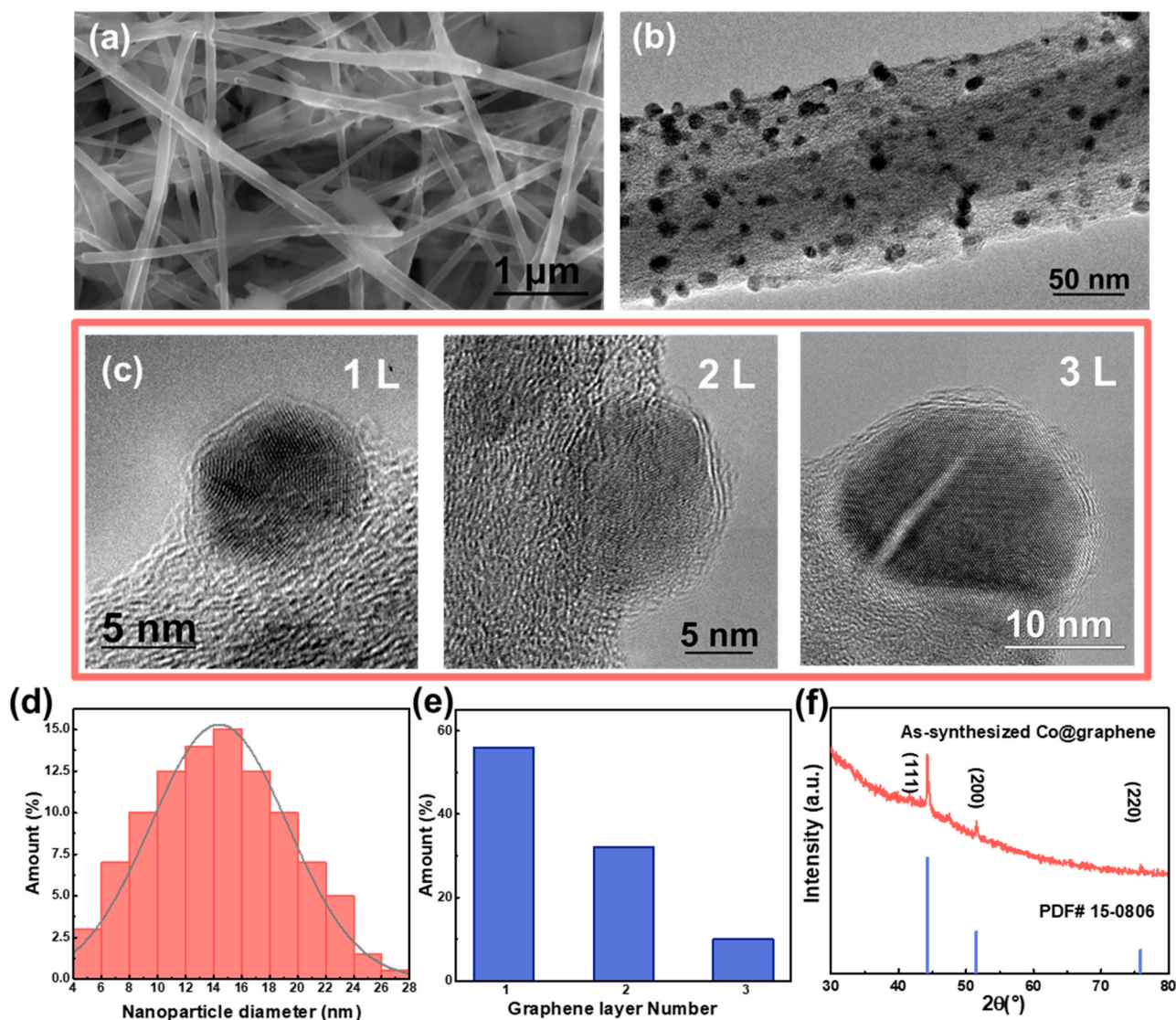


Fig. 1. Schematic demonstrating the high-temperature-pulse method to controllably synthesize core-shell nanoparticles, such as Co@graphene, with one to three graphene coating layers.



**Fig. 2.** Characterization of the Co@graphene nanoparticles: formation and morphology. (a) Scanning electron microscope (SEM) image of the CNF film loaded with the cobalt precursor salt. (b) Low-magnification TEM image of the Co@graphene nanoparticle anchored onto the CNF substrate. (c) TEM images showing graphene coatings composed of 1–3 layers, respectively, on Co nanoparticles. (d) Distribution plot showing the range of Co nanoparticle diameters. (e) Graphene coating layer distribution plot for the core-shell Co@graphene nanoparticles. (f) XRD pattern for the Co@graphene core-shell nanoparticles.

pyridinic N, as well as the decrease of graphitic N.

This one-step strategy for synthesis of graphene protected nanoparticles also presents its universality, which can be applied to other transition metal elements as well. Fig. 4a, b and S8 present the TEM morphologies and XRD patterns of iron and nickel-based nanoparticles whose structures and dimensions show similar results to the Co@graphene nanoparticles. Besides, there is a broad range of carbon-based substrates that enable this high temperature pulsing technique. Apart from two-dimensional (2D) CNF thin film (Fig. 4c), a block of three-dimensional (3D) carbonized wood can also function as the substrate to generate core-shell nanoparticles. The 3D carbonized wood layer consists of aligned open channels (diameter of tens of micrometers) that can act as a chamber to accommodate the pristine salt and the deposition surface where the as-formed core-shell nanoparticles can get anchored (Fig. 4d and S9). The SEM images shows that all the channels are filled with the homogeneously dispersed Co@graphene nanoparticles. The inexpensive wood substrate can be utilized as a large-scale manufacture substrate, which can tremendously increase the loading amount of nanoparticles with a facile large scale manufacturing.

As a demonstration of the functional applications, we performed

electrocatalytic studies on the graphene-coated Co nanoparticles (denoted as N-Co@graphene and Co@graphene) for the oxygen reduction reaction (ORR). As a control, Co nanoparticle supported on high-surface-area carbon black (denoted as Co/C, see method section for the details of catalyst preparation) was also evaluated under similar conditions. The electrocatalytic studies were performed using the rotating disk electrode (RDE) method in 0.1 M KOH. Fig. 5a shows the voltammograms recorded in argon and oxygen-saturated electrolytes. When the electrolyte is saturated with O<sub>2</sub>, a pronounced oxygen-reduction peak appears in the cathodic scan. The onset potential of this peak is positively shifted for N-Co@graphene and Co@graphene as compared to Co/C. Correspondingly, the peak current for N-Co@graphene and Co@graphene was also found to be as high as 1.5 – 1.7 times of that for Co/C. These results indicate that graphene coated cobalt nanoparticles are more active than Co/C, which is further confirmed by the ORR polarization curves (Fig. 5b). The more facile reaction kinetics of N-Co@graphene was confirmed by its low Tafel slope in kinetic region (Fig. 5c).

First-principles density functional theory (DFT) calculations reveal that the graphene coated Co structure contributes to the overall activity.

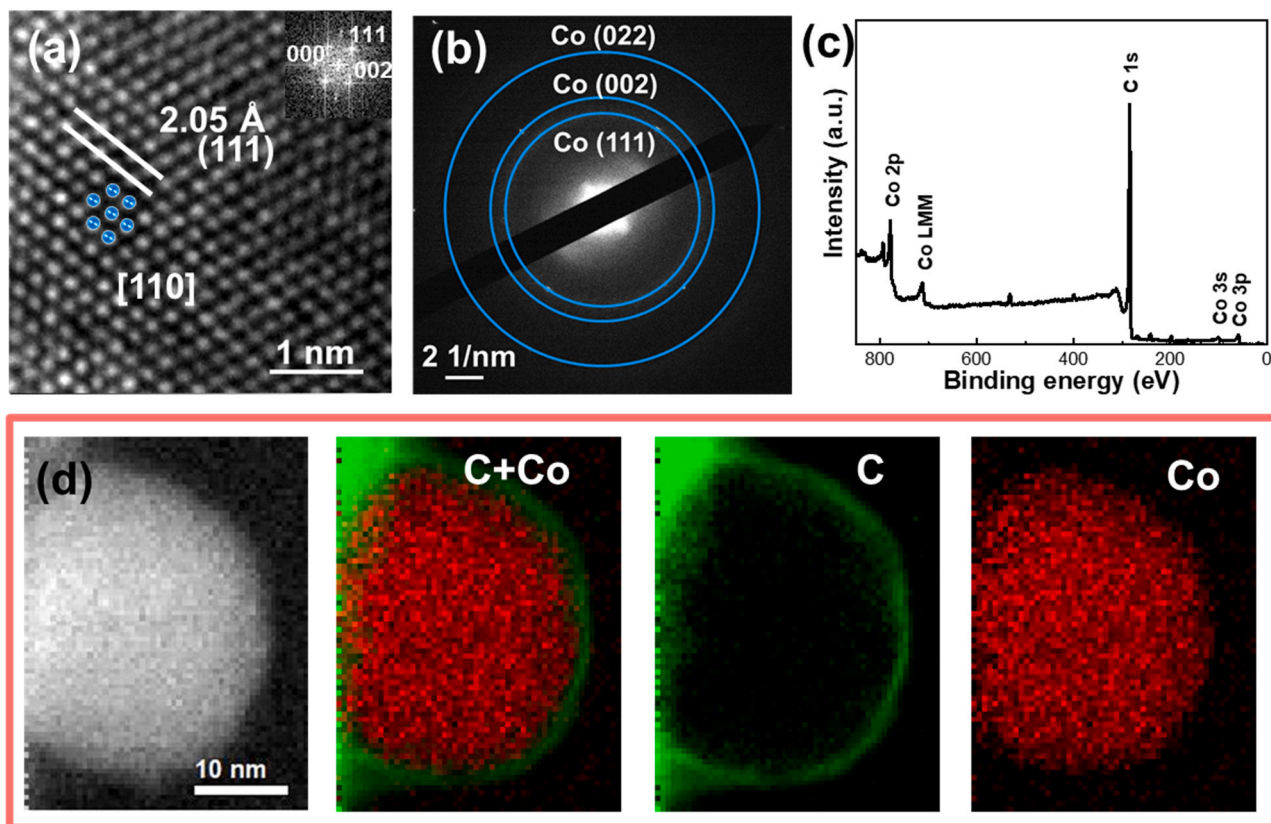


**Fig. 3.** Compositional analysis of the Co@graphene nanoparticles. (a) HR-TEM analysis of the lattice of nanoparticles. (b) Selected area electron diffraction pattern shows the fcc structure of Co nanoparticles. (c) XPS spectrum of the supported Co@graphene core-shell nanoparticles. (d) STEM-EELS maps of the core-shell nanoparticles.

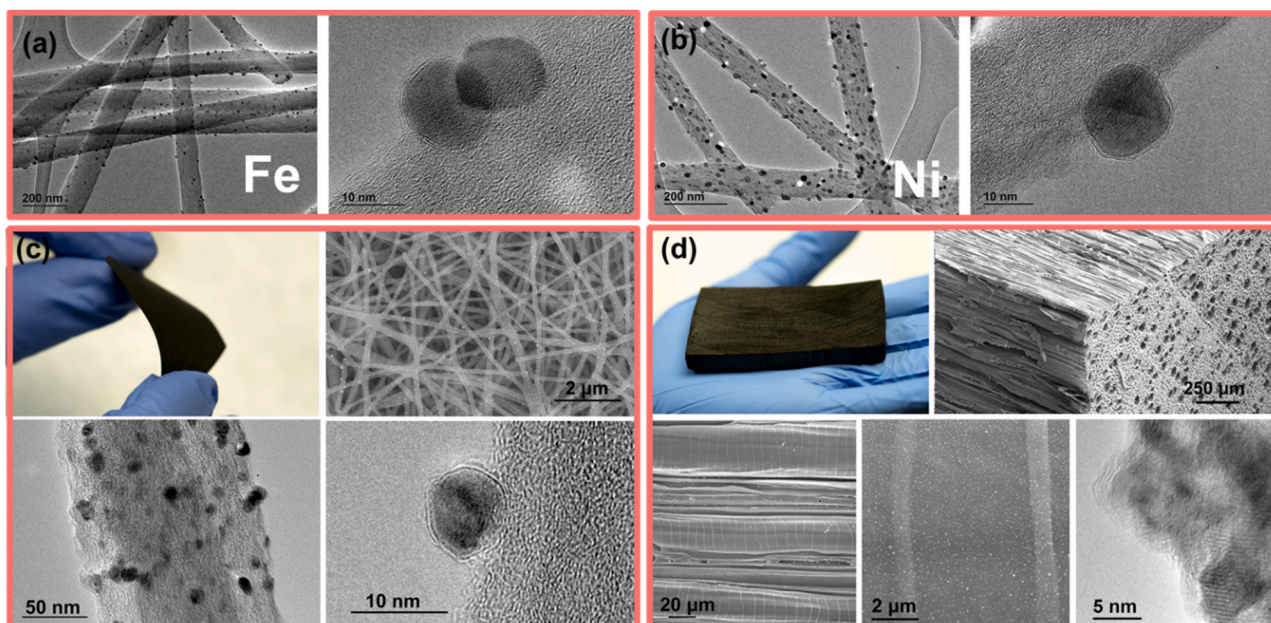


**Fig. 4.** (a) Morphology of iron@graphene core-shell nanoparticles. (b) Morphology of nickel@graphene core-shell nanoparticles. (c) CNF as the supported substrate (d) Carbonized wood as the supported substrate.

The synergy between the metallic Co core and the ultrathin graphene coating (1 at. layer) can account for the activity. We have modelled the Co@graphene catalysts as a perfect graphene layer on top of a four-atom tetrahedral Co cluster (Fig. 5d). The calculated charge density difference

map (Fig. 5e) shows that the carbon atoms adjacent to the Co cluster would have lower electron density than the carbon atoms in other regions. Especially, the carbon atom marked with the dashed circle in the figure was found to exhibit the greatest degree of electron density

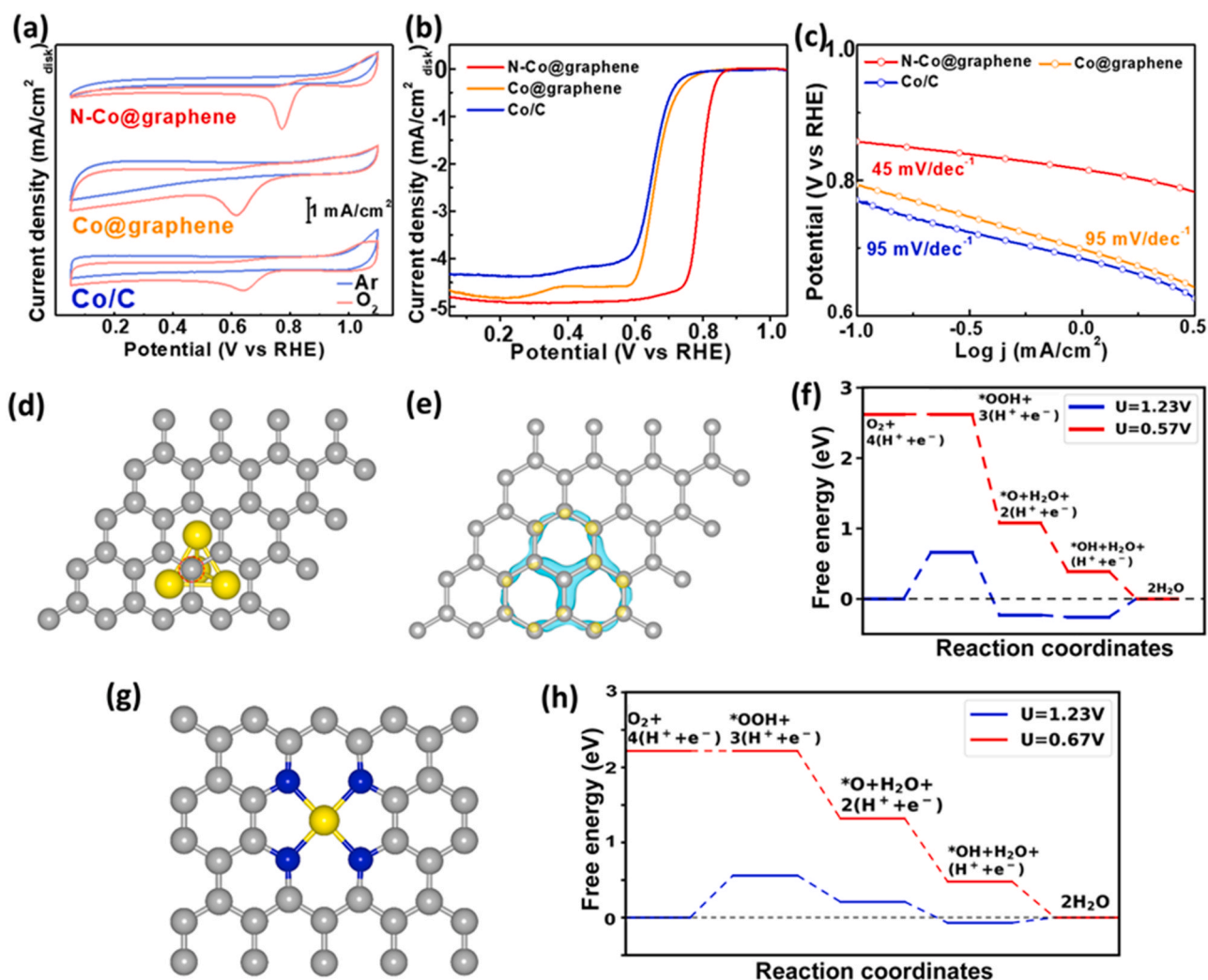


**Fig. 5.** (a) Voltammograms for N-Co@graphene, Co@graphene and Co/C in Ar- and O<sub>2</sub>-saturated 0.1 M KOH. (b) ORR polarization curves at 1600 rpm and (c) corresponding Tafel plots. (d) Structure of a graphene layer in contact with a four-atom Co cluster, which was used to model Co@graphene catalysts. The gray balls represent C atoms and the yellow balls represent Co atoms. (e) Predicted electron density change on the carbon atoms induced by the local contact between Co cluster and graphene layer. Isosurface level is set as  $0.05e^{-3}$ . Color yellow and cyan indicate electron accumulation and depletion, respectively. (f) Calculated free energy evolution diagram for the ORR through 4e<sup>-</sup> associative pathway on Co@graphene. (g) Atomic structure of fully embedded Co-N-C moiety in graphene. In the figure, the gray, blue, and yellow balls represent C, N, and Co atoms, respectively. (h) Calculated free energy evolution diagram for the ORR through 4e<sup>-</sup> associative pathway on N-Co@graphene. (For interpretation of the references to colour in this figure legend, the reader is referred to the web version of this article.)

depletion and act as active site of the catalyst for ORR. We have predicted the configurations (Fig. S11) and energies (Table S1) of ORR species adsorbed on the top of this active site. We applied the computational hydrogen electrode method developed by Nørskov et al. [25] to calculate the free energy evolution of a four-electron (4e<sup>-</sup>) ORR pathway on the Co cluster induced active carbon (Fig. 4f). When the electrode potential  $U$  is lower than a limiting potential of 0.57 V, all the elementary reactions involving charge-transfer become exergonic and thermodynamically favorable on the active carbon. The result is consistent with previous results about stabilization of oxygenated adsorbates [26–31]. This synergic effect can also explain the stability and durability of nanoparticles, since there is no direct contact between Co and O atoms in the ORR process, in which the graphene layer acts as an electron messenger involved in the interactions between Co and O atoms. The experimental result confirmed the durable Co@graphene structure with negligible degradation after 3000 potential cycles (Fig. S12), comparable to some of the precious metal-based electrocatalysts [32,33]. To further understand the effect of doping nitrogen treatment, a fully embedded Co-N-C moiety (Fig. 5g, S14) was proposed as a possible active site for N-Co@graphene in the DTF model. The free energy

evolution (Fig. 5h) was obtained following same 4e<sup>-</sup> ORR associative path. The limiting potential of 0.67 V is higher than the one of Co@graphene, which agrees well with experimental trend that the onset potential of N-Co@graphene is more positive than Co@graphene [34].

In conclusion, we report a one-step synthetic technique to fabricate supported Co@graphene core-shell nanoparticles. This strategy presents several advantages, such as generation of core-shell nanostructures in one facile processing step, tunability and control over graphene shell thickness down to monolayer graphene, as well as the abundance of substrate candidates. The ORR test of the supported Co@graphene sample presented its activity and durability, and DFT calculations illustrates that the local contact between Co core and graphene shell produces carbon atoms with lower electron density, which help effectively improve the ORR activity. This facile synthetic approach provides a pathway towards the design and development of metal/graphene core-shell nanoparticles with controllable graphene coating thickness for a wide range of potential applications in the fields of catalysis and beyond.

## 2. Methods

### 2.1. Preparation of CNF

An 8% by mass solution of polyacrylonitrile (PAN) (Sigma Aldrich) in dimethylformamide (DMF) was electrospun at a voltage of 10 kV, a spinning distance of 15 cm, and a feeding rate of 1 mL/hour. The as-spun nanofibers were collected by a rotation drum at a speed of 80 rpm. The electrospun film was then converted into CNFs after stabilizing in air at 280 °C for 5 h and carbonizing at 600 °C in an argon atmosphere.

### 2.2. Fabrication process of supported core-shell nanoparticles

Cobalt (II) chloride (CoCl<sub>2</sub>·0.6 H<sub>2</sub>O) salt was dissolved in ethanol to form a 0.05 mmol/mL solution. The precursor solution was dropped onto the CNF or carbonized wood substrate in a controlled manner. The as-prepared film was then connected to copper electrodes and silver paste was employed to glue the carbon substrate to the electrodes. A high temperature pulse was applied to the substrate in an argon-filled glovebox using an external Keithley 2425 Source Meter. The emitted light from the substrate was collected by a high-speed spectrometer camera and fitted using the blackbody radiation equation.

The emission spectrum of the CNF film during the high temperature pulse was recorded with a high-speed camera, from which the temperature can be evaluated through black-body radiation analysis. The light emission intensity during the pulse period and the corresponding temperature vs. time curves including the heating and cooling process can be also be acquired (Fig. S1).

### 2.3. Preparation of Co/C control sample

Co nanoparticles were synthesized following a slightly modified reported method [35]. Briefly, 100 μl oleic acid, 160 μl dioctylamine and 15 mL of dichlorobenzene were slowly heated to boiling point of dichlorobenzene (~ 182 °C). To this solution, 100 mg of dicobalt octacarbonyl dissolved in 3 mL dichlorobenzene were injected. The mixture was kept at ~ 182 °C for 15 min before cooled down to room temperature. Co nanoparticles were recovered by adding ethanol and centrifuging. The sediment was dispersed in toluene before adding ethanol and centrifuging again. The resulting product was dispersed in toluene. To make the Co/C catalyst, high surface area carbon (Tanaka Inc.) was added into cobalt dispersion before ultrasonication for 30 min. Cobalt weight loading on carbon was controlled to be ~ 18% to be consistent with Co@graphene. To remove organic surfactant on Co, ethanol was added into the above dispersion before it was centrifuged. Sediment was dispersed in hexane and centrifuged again. Co/C catalyst was acquired by drying sediment under vacuum for 20 min.

### 2.4. Materials characterization

The low-magnification morphological images of the carbon substrates were acquired using a field-emission SEM (Tescan XEIA FEG SEM). TEM at an accelerating voltage of 200 kV was used to characterize the nanoparticle morphologies at high resolution. Atomic resolution TEM images as well as EELS maps were also obtained. XPS analysis was performed on a multi-technique photoelectron spectrometer with a standard dual (Mg/Al) anode and monochromatic (Al) X-ray sources. The XRD pattern in Supporting Information for the control sample was achieved by PANalytical X'Pert Powder X-Ray Diffractometer. All other XRD patterns were achieved using a D8 Bruker Advanced X-ray Diffraction system.

### 2.5. Electrode preparation

Both Co@graphene and Co/C were mixed in aqueous solvent

containing 0.05% Nafion and 10% isopropanol with a concentration of 1 mg/mL. The mixture was ultrasonicated for at least 30 min to achieve a homogeneous ink. The ink was then drop-casted onto a 5 mm diameter glassy carbon rotating disk electrode and allowed to dry to form a uniform catalyst film. Total catalyst loading, including the Co and carbon, was 0.2 mg/cm<sup>2</sup> disk.

### 2.6. Electrochemical measurements

Electrochemical tests were conducted with a Metrohm Autolab PGSTAT302N potentiostat connected to a three-electrode cell made with Teflon. Hg/HgO and platinum wire were adopted as the reference and counter electrodes, respectively. 60 mL of 0.1 M KOH was prepared with de-ionized water and implemented as the electrolyte. Polarization curves were measured with a scan rate of 50 mV/s.

The electron transfer number during ORR was calculated based on the Koutecky-Levich equation:

$$\frac{1}{j} = \frac{1}{j_L} + \frac{1}{j_K} = \frac{1}{B\omega^{1/2}} + \frac{1}{j_K}$$

where  $j$ ,  $j_L$ ,  $j_K$  are nominal, diffusion limiting and kinetic current density, respectively. The reverse of the K-L plot slope,  $B$ , is:

$$B = 0.2nF\nu^{-1/6}C_0D_0^{2/3}$$

where  $n$  is the electron transfer number,  $F$  is the Faraday constant (96,485 C/mol),  $\nu$  is the kinetic viscosity (0.01 cm<sup>2</sup>/s),  $C_0$  is the concentration of oxygen within the electrolyte (1.2 mmol/L), and  $D_0$  is the diffusion coefficient of oxygen within the electrolyte ( $1.9 \times 10^{-5}$  cm<sup>2</sup>/s).

Accelerated stability tests were conducted by cycling the electrode between 0.6 V and 1.0 V (vs RHE) at 50 mV/s in an oxygen-saturated electrolyte.

### 2.7. Computational method

The first-principles spin-polarized density functional theory (DFT) calculations [36,37] were performed using Vienna ab-initio Simulation Package (VASP) [38]. Projector augmented wave (PAW) pseudopotential [39,40] was used to describe the core electrons and energy cutoff was set as 400 eV to expand the wave function. The Perdew-Burke-Ernzerhof (PBE) functionals [41] were used to describe the exchange-correlation effects. The atomic structures were optimized until the force was below 0.01 eV/Å. The Brillouin zone was sampled with Monkhorst-pack [42]  $4 \times 4 \times 1$  k-points grids. A vacuum region of 14 Å was added into the simulation cell to avoid the interaction between two adjacent images. Zero-point energy (ZPE) corrections were included in all the reported adsorption energies. The transition states of chemical reaction were located using the climbing image nudged elastic band (CI-NEB) method, in which the force along and perpendicular to the reaction path were relaxed to less than 0.05 eV/Å.

### CRediT authorship contribution statement

**Hua Xie:** Conceptualization, Methodology, Investigation, Writing - original draft. **Yifan Liu:** Conceptualization, Methodology, Investigation, Writing - original draft. **Na Li:** Investigation. **Boyang Li:** Formal analysis, Writing - original draft. **Yonggang Yao:** Investigation. **Michael R. Zachariah:** Supervision. **Guofeng Wang:** Supervision, Writing - review & editing. **Dong Su:** Supervision, Writing - review & editing. **Chao Wang:** Supervision, Writing - review & editing. **Liangbing Hu:** Conceptualization, Methodology, Supervision, Writing - review & editing.

### Declaration of Competing Interest

The authors declare that they have no known competing financial

interests or personal relationships that could have appeared to influence the work reported in this paper.

## Acknowledgements

We acknowledge the support of the Maryland Nanocenter, its Surface Analysis Center and AIMLab. Electron Microscopy (EM) work used resources of the Center for Functional Nanomaterials, which is a US DOE Office of Science Facility, at Brookhaven National Laboratory under Contract No. DE-SC0012704.

## Appendix A. Supporting information

Supplementary data associated with this article can be found in the online version at [doi:10.1016/j.nanoen.2020.105536](https://doi.org/10.1016/j.nanoen.2020.105536).

## References

- Z. Deng, Y. Tian, S. Lee, A.E. Ribbe, C. Mao, DNA-encoded self-assembly of gold nanoparticles into one-dimensional arrays, *Angew. Chem. Int. Ed.* 44 (2005) 3582–3585.
- P.G. Bruce, B. Scrosati, J.M. Tarascon, Nanomaterials for rechargeable lithium batteries, *Angew. Chem. Int. Ed.* 47 (2008) 2930–2946.
- H. Lai, L. Shang, Q. Wu, L. Yang, J. Zhao, H. Li, Z. Lyu, X. Wang, Z. Hu, Spinel nickel cobaltite mesostructures assembled from ultrathin nanosheets for high-performance electrochemical energy storage, *ACS Appl. Energy Mater.* 1 (2018) 684–691.
- L. Huang, D. Santiago, P. Loyselle, L. Dai, Small 1800879 (2018) 1–11.
- L. Luo, M.H. Engelhard, Y. Shao, C. Wang, Revealing the dynamics of platinum nanoparticle catalysts on carbon in oxygen and water using environmental TEM, *ACS Catal.* 7 (2017) 7658–7664.
- X. Ge, Y. Du, B. Li, T.S.A. Hor, M. Sindoro, Y. Zong, H. Zhang, Z. Liu, Intrinsically conductive perovskite oxides with enhanced stability and electrocatalytic activity for oxygen reduction reactions, *ACS Catal.* 6 (2016) 7865–7871.
- Z. Weng, Y. Wu, M. Wang, J. Jiang, K. Yang, S. Huo, X.F. Wang, Q. Ma, G. W. Brudvig, V.S. Batista, Y. Liang, Z. Feng, H. Wang, Structural absorption by barbule microstructures of super black bird of paradise feathers, *Nat. Commun.* 9 (2018) 1–9.
- P. Liu, Y. Zhao, R. Qin, S. Mo, G. Chen, L. Gu, D.M. Chevrier, P. Zhang, Q. Guo, D. Zhang, Photochemical route for synthesizing atomically dispersed palladium catalysts, *Science* 352 (2016) 797–800.
- D.Y. Chung, S.W. Jun, G. Yoon, S.G. Kwon, D.Y. Shin, P. Seo, J.M. Yoo, H. Shin, Y.-H. Chung, H. Kim, Highly durable and active PtFe nanocatalyst for electrochemical oxygen reduction reaction, *J. Am. Chem. Soc.* 137 (2015) 15478–15485.
- H. Hata, S. Kubo, Y. Kobayashi, T.E. Mallouk, Intercalation of well-dispersed gold nanoparticles into layered oxide nanosheets through intercalation of a polyamine, *J. Am. Chem. Soc.* 129 (2007) 3064–3065.
- M.E. Strayer, J.M. Binz, M. Tanase, S.M. Kamali Shahri, R. Sharma, R.M. Rioux, T. E. Mallouk, Interfacial bonding stabilizes rhodium and rhodium oxide nanoparticles on layered nb oxide and ta oxide supports, *J. Am. Chem. Soc.* 136 (2014) 5687–5696.
- P.N. Duchesne, Z.Y. Li, C.P. Deming, V. Fung, X. Zhao, J. Yuan, T. Regier, A. Aldabahi, Z. Almarhoon, S. Chen, D. en Jiang, N. Zheng, P. Zhang, Golden single-atomic-site platinum electrocatalysts, *Nat. Mater.* 17 (2018) 1033–1039.
- Y. Sun, X. Zhang, M. Luo, X. Chen, L. Wang, Y. Li, M. Li, Y. Qin, C. Li, N. Xu, G. Lu, P. Gao, S. Guo, *Adv. Mater.* 30 (2018) 1–8.
- Z. Zhang, G. Liu, X. Cui, B. Chen, Y. Zhu, Y. Gong, F. Saleem, S. Xi, Y. Du, A. Borgna, Z. Lai, Q. Zhang, B. Li, Y. Zong, Y. Han, L. Gu, H. Zhang, Electrodeposition: electrocarving during electrodeposition growth (*Adv. Mater.* 51/2018), *Adv. Mater.* 30 (2018) 1–7.
- S. Guo, S. Zhang, L. Wu, S. Sun, Co/CoO nanoparticles assembled on graphene for electrochemical reduction of oxygen, *Angew. Chem. Int. Ed.* 51 (2012) 11770–11773.
- D. Kim, N. Becknell, Y. Yu, P. Yang, Room-temperature dynamics of vanishing copper nanoparticles supported on silica, *Nano Lett.* 17 (2017) 2732–2737.
- L. Du, L. Luo, Z. Feng, M. Engelhard, X. Xie, B. Han, J. Sun, J. Zhang, G. Yin, C. Wang, Nitrogen-doped graphitized carbon shell encapsulated NiFe nanoparticles: a highly durable oxygen evolution catalyst, *Nano Energy* 39 (2017) 245–252.
- Z. Zhang, J. Sun, F. Wang, L. Dai, Efficient oxygen reduction reaction (ORR) catalysts based on single iron atoms dispersed on a hierarchically structured porous carbon framework, *Angew. Chem. Int. Ed.* 57 (2018) 9038–9043.
- Q. Cheng, S. Han, K. Mao, C. Chen, L. Yang, Z. Zou, M. Gu, Z. Hu, H. Yang, Co nanoparticle embedded in atomically-dispersed Co-N-C nanofibers for oxygen reduction with high activity and remarkable durability, *Nano Energy* 52 (2018) 485–493.
- Z. Li, Z. Zhuang, F. Lv, H. Zhu, L. Zhou, M. Luo, J. Zhu, Z. Lang, S. Feng, W. Chen, L. Mai, S. Guo, *Adv. Mater.* 1803220 (2018) 1–8.
- H. Rui, R. Xing, Z. Xu, Y. Hou, S. Goo, S. Sun, Synthesis, functionalization, and biomedical applications of multifunctional magnetic nanoparticles, *Adv. Mater.* 22 (2010) 2729–2742.
- G. Prieto, J. Zečević, H. Friedrich, K.P. De Jong, P.E. De Jongh, Towards stable catalysts by controlling collective properties of supported metal nanoparticles, *Nat. Mater.* 12 (2013) 34–39.
- S. Bhaviripudi, X. Jia, M.S. Dresselhaus, J. Kong, Role of kinetic factors in chemical vapor deposition synthesis of uniform large area graphene using copper catalyst, *Nano Lett.* 10 (2010) 4128–4133.
- C. Film, H. Ago, Y. Ito, N. Mizuta, K. Yoshida, B. Hu, C.M. Orofeo, Epitaxial chemical vapor deposition growth of single-layer graphene over cobalt film crystallized on sapphire, *ACS Nano* 4 (2010) 7407–7414.
- J.K. Nørskov, J. Rossmeisl, A. Logadottir, L. Lindqvist, D. Lyngby, H. Jo, Origin of the overpotential for oxygen reduction at a fuel-cell cathode, *J. Phys. Chem. B* 108 (2004) 17886–17892.
- M. Kim, D.-H. Nam, H.-Y. Park, C. Kwon, K. Eom, S. Yoo, J. Jang, H.-J. Kim, E. Cho, H. Kwon, Cobalt-carbon nanofibers as an efficient support-free catalyst for oxygen reduction reaction with a systematic study of active site formation, *J. Mater. Chem. A* 3 (2015) 14284–14290.
- V.V.T. Doan-Nguyen, S. Zhang, E.B. Trigg, R. Agarwal, J. Li, D. Su, K.I. Winey, C. B. Murray, Synthesis and X-ray characterization of cobalt phosphide (Co<sub>2</sub>P) nanorods for the oxygen reduction reaction, *ACS Nano* 9 (2015) 8108–8115.
- S. Jiang, C. Zhu, S. Dong, Cobalt and nitrogen-cofunctionalized graphene as a durable non-precious metal catalyst with enhanced ORR activity, *J. Mater. Chem. A* 1 (2013) 3593.
- Y. Hu, J.O. Jensen, W. Zhang, L.N. Cleemann, W. Xing, N.J. Bjerrum, Q. Li, Hollow spheres of iron carbide nanoparticles encased in graphitic layers as oxygen reduction catalysts, *Angew. Chem. Int. Ed.* 53 (2014) 3675–3679.
- J. Deng, P. Ren, D. Deng, X. Bao, Enhanced electron penetration through an ultrathin graphene layer for highly efficient catalysis of the hydrogen evolution reaction, *Angew. Chem. Int. Ed.* 54 (2015) 2100–2104.
- J. Deng, D. Deng, X. Bao, *Adv. Mater.* 29 (2017) 1–23.
- X.X. Wang, D.A. Cullen, Y. Pan, S. Hwang, M. Wang, Z. Feng, J. Wang, M. H. Engelhard, H. Zhang, Y. He, Nitrogen-coordinated single cobalt atom catalysts for oxygen reduction in proton exchange membrane fuel cells, *Adv. Mater.* 30 (2018), 1706758.
- X. Huang, Z. Zhao, L. Cao, Y. Chen, E. Zhu, Z. Lin, M. Li, A. Yan, A. Zettl, Y. M. Wang, X. Duan, T. Mueller, Y. Huang, High-performance transition metal-doped Pt<sub>3</sub>Ni octahedra for oxygen reduction reaction, *Science* 348 (2015) 1230–1234.
- T.S. Olson, S. Pyllypenko, P. Atanassov, K. Asazawa, K. Yamada, H. Tanaka, Anion-exchange membrane fuel cells: dual-site mechanism of oxygen reduction reaction in alkaline media on cobalt–polypyrrole electrocatalysts, *J. Phys. Chem. C* 114 (2010) 5049–5059.
- Y. Bao, W. An, C. Heath Turner, K.M. Krishnan, The critical role of surfactants in the growth of cobalt nanoparticles, *Langmuir* 26 (2010) 478–483.
- P. Hohenberg, W. Kohn, Inhomogeneous electron gas, *Phys. Rev.* 136 (1964) B864–B871.
- W. Kohn, L.J. Sham, Self-consistent equations including exchange and correlation effects, *Phys. Rev.* 140 (1965) A1133–A1138.
- G. Kresse, J. Furthmüller, Efficiency of ab-initio total energy calculations for metals and semiconductors using a plane-wave basis set, *Comput. Mater. Sci.* 6 (1996) 15–50.
- P.E. Blöchl, Projector augmented-wave method, *Phys. Rev. B* 50 (1994) 17953–17979.
- G. Kresse, D. Joubert, From ultrasoft pseudopotentials to the projector augmented-wave method, *Phys. Rev. B* 59 (1999) 1758–1775.
- J.P. Perdew, K. Burke, M. Ernzerhof, Generalized gradient approximation made simple, *Phys. Rev. Lett.* 77 (1996) 3865–3868.
- H.J. Monkhorst, J.D. Pack, Special points for Brillouin-zone integrations, *Phys. Rev. B* 13 (1976) 5188–5192.